Refractive Index Sensing Simulations of $CsPbBr_3$ Quantum Dots/Gold Bilayer Coated Triangular-Lattice Photonic Crystal Fibers

Ye TAO[1], Han YE[2], Yong DING[1], Xiaomin REN[2], and Xiaolong LIU[1*]

[1]*School of New Energy, North China Electric Power University, Beijing 102206, China*

[2]*State Key Laboratory of Information Photonics and Optical Communications, University of Posts and Telecommunications, Beijing 100876, China*

[*]Corresponding author: Xiaolong LIU E-mail: xl.liu@ncepu.edu.cn

Abstract: With the incorporation of noble metal materials, photonic crystal fibers (PCFs) could be performed as an effective platform for refractive index sensing of the filling analytes. Furthermore, by coating functional dielectric layers upon the metal surfaces, the resonance energy transfer is modulated from the core mode of the PCFs towards the surface plasmon resonance mode of the metals, and the sensing performance could be boosted. Here, considering that the exciton-plasmon coupling is efficient between perovskite quantum dots (QDs) and gold, a kind of $CsPbBr_3$ QDs/Au bilayer coated triangular-lattice PCFs has been simulated numerically as the refractive index sensors. With the optimization of the QDs and gold layer thicknesses, together with the variation of the central hole size of the PCFs, in the refractive index (RI) region of 1.26 to 1.34, a rather narrow full width at half maximum (FWHM) of the loss spectra was achieved as 13.74 nm when the central hole size was 1.28 μm and the highest figure of merit was 63.79 RIU (the central hole size was 1.53 μm). This work demonstrates that the analyte identification accuracy was enhanced by FWHM narrowing of the loss spectra; in addition, taking the abundance of the material choice of perovskite QDs into consideration, more analytes could be detected effectively. Moreover, by adopting asymmetric structures, the sensitivity of the PCFs based refractive index sensors could be further improved.

Keywords: Photonic crystal fibers; perovskite quantum dots; refractive index sensor; narrow FWHM

Citation: Ye TAO, Han YE, Yong DING, Xiaomin REN, and Xiaolong LIU, "Refractive Index Sensing Simulations of $CsPbBr_3$ Quantum Dots/Gold Bilayer Coated Triangular-Lattice Photonic Crystal Fibers," *Photonic Sensors*, 2022, 12(3): 220309.

Open Science Identity (OSID)

1. Introduction

With noble metals coated on the cladding holes, grooves, or side polished surfaces of photonic crystal fibers (PCFs), attributed to the coupling of the transmitted electromagnetic wave with the charge-density oscillation on the metal surfaces, a strong resonance loss occurs for the core mode with its energy transferred to the surface plasmon resonance (SPR) mode of the metals [1]. At certain wavelengths, resonance takes place only if the propagation constants of the core mode match with the SPR mode, which could be modulated by the permittivity of the metal, the refractive index (RI) of

Received: 8 April 2021 / Revised: 19 July 2021

DOI: 10.1007/s13320-022-0641-1
Article type: Regular

the surrounding dielectric materials, and the configuration of the PCFs. Consequently, with the RI of the dielectric material changing, e.g., to fill the air holes of a metal-coated PCF with different analytes, the resonance loss appears at different wavelengths [2–4]. From this aspect, metal-coated PCFs could act as effective platforms for RI sensing and have been studied intensively [5–11]. Among the noble metal coating materials, gold and silver are mostly adopted with high SPR intensity in the visible light region [12], and gold is even preferable for its chemical stability. However, gold-based PCF RI sensors always exhibit wide full width at half maximum (FWHM) from the loss spectra, which decreases the accuracy to distinguish the filled analytes with different RIs (or n_a). Specially designed PCF structures could compensate this shortcoming [13–18], though the accompanied infrared working region for some PCFs makes it inconvenient for practical operations [15, 16].

Furthermore, it has been found that coating dielectric layers onto the metal films could be an effective strategy to improve the performance of Au-based PCF RI sensors. Erdmanis *et al.* [3] applied TiO_2 films upon Au to achieve a sensitivity larger than 4600 nm per refractive index unit (RIU), and the FWHM was only 10 nm – 20 nm, though the resonance wavelength was beyond the visible region (1500 nm – 1600 nm). Graphene was also adopted as the dielectric coating material in the D-shaped PCF, a kind of PCF with one polished surface along the light propagation direction, and the sensitivity was improved. The FWHM, however, was more than 50 nm [19]. Additionally, with numerical analysis, by sandwiching a gold film between two different dielectric layers in the grooves of H-shaped PCFs (a kind of PCF with the cladding silica and air holes replaced by two symmetric grooves), after the optimizations of the RI and the thickness of the dielectric layers, a high sensitivity of more than 2 000 nm/RIU and an FWHM of less than 30 nm could be achieved [20].

Recently, lead halide perovskite quantum dots (QDs) have been studied extensively due to the outstanding optoelectronic properties in the whole visible light region. What's more, the perovskite QDs possess high extinction coefficient and effective exciton-plasmon coupling ability with Au [21–23], which implies that a hetero-structured coating layer of perovskite QDs and Au could efficiently improve the performance of PCF-based RI sensors by boosting the energy transfer from the core mode toward the Au layer at resonance wavelengths. Besides, among lead halide perovskites, $CsPbBr_3$ QDs exhibit the best humid and thermal tolerant abilities, satisfying the requirements of the dielectric coating materials on Au in the PCF RI sensors.

In this work, we performed the RI sensing simulations of triangular-lattice PCFs coated with $CsPbBr_3$ QDs upon Au layers on the sidewalls of the central holes, which was then referred as "QDs/Au sensors". Compared to the PCFs covered with only Au layers in the same structure (shortened as "Au sensors"), the incorporation of the $CsPbBr_3$ QDs layers effectively improved the amplitude sensitivity, wavelength sensitivity, and FWHM of the loss spectra in the RI range of 1.26 – 1.34 for different filling analytes, and the working region was within visible spectra. Besides, geometric parameters including the layer number of the QDs, the thickness of the Au layer, and the diameter of the central holes were adjusted to explore their influences on the sensitivities and FWHM. The best results were obtained with the diameter of the central holes as 1.53 μm, coated with 30-nm-thick Au and 2 layers of QDs (each layer of the QDs was 10-nm-thick), showing 947 nm/RIU wavelength sensitivity, 15.48 nm FWHM, and 63.79 RIU^{-1} figure of merit (FOM) for n_a = 1.30. With the change of the central hole sizes, FWHM was further narrowed as 13.74 nm. The QDs/Au sensors in this work exhibited a quite small FWHM value compared to nearly 100 nm FWHM of previously reported sensors for the RI

range of 1.26 – 1.34 [24–26]. The QDs/Au sensors could be applicable for organic solvent identifications with low RIs or temperature detections combining with temperature sensitive analytes [27, 28]. It is expected that with a rational design of the PCF structures, the performance of the QDs/Au sensors could be further improved.

2. Structural design and numerical modelling

The schematic illustration of a triangular-lattice PCF is shown in Fig. 1(a). The diameter of the central air holes and the distance between the adjacent holes were D = 1.53 μm and L = 2.55 μm, respectively. The sidewalls of the central air holes were firstly covered with 30-nm-thick Au layers, followed with the coating of 2 layers of $CsPbBr_3$ QDs (the thickness of each QD layer was 10 nm). It must be mentioned that the size of the $CsPbBr_3$ QDs was 10 nm (with the extinction properties studied in [21]), then the thickness of each QD layer was assumed ideally as also 10 nm, considering that the QDs with this size were roughly cubic shaped and small enough to be self-assembled as a uniform coating layer upon the Au layers. The rest space of the central holes was filled by analytes with different RIs. The other holes in the PCF had the same diameter with the central holes which were filled with only air and no Au or QDs layer was coated on. For comparison, PCFs with the central holes coated only by 30-nm-thick Au layers in the same geometric structure have also been investigated.

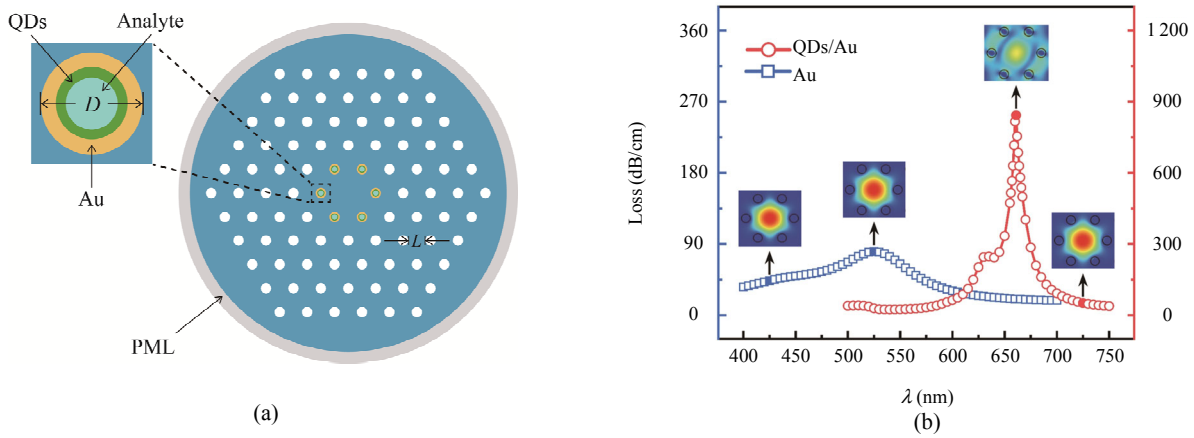

Fig. 1 Structure and device performance of the QDs/Au sensors: (a) schematic of the PCF RI sensor coated with the Au and QDs film in the central holes and (b) loss spectra of the core mode for a QDs/Au sensor and an Au sensor. Inset: electric field distributions for the Au sensor at 425 nm and 525 nm (resonance wavelength), and for the QDs/Au sensor at 660 nm (resonance wavelength) and 725 nm with n_a = 1.30.

The PCF material was fused silica and the RI was evaluated by the Sellmeier equation:

$$n^2(\lambda) = 1 + \sum_i^3 \frac{B_i \lambda^2}{\lambda^2 - C_i} \tag{1}$$

where B_i and C_i are Sellmeier coefficients in [29] as shown in Table 1, and λ represents the wavelength of the incident light through the core of the PCF, in the unit of μm.

The RI of air was set to be 1, and the dielectric constant of Au was given by the Drude-Lorentz model:

$$\varepsilon(k) = 1 + \sum_i \frac{\Delta\varepsilon_i}{-k^2 + a_i(ik) + b_i} \tag{2}$$

where $\Delta\varepsilon_i$, a_i, and b_i are the coefficients to fit the real permittivity of Au [8], as listed in Table 2, and $k = 2\pi/\lambda$ is the wavenumber in the unit of cm^{-1}.

Table 1 Parameters of fused silica for Sellmeier equation.

i	B_i	C_i
1	0.696 163	0.004 679 15
2	0.407 943	0.013 512 1
3	0.897 479	97.934 0

Table 2 Parameters of Au in Drude-Lorentz model.

i	$\Delta\varepsilon_i$	a_i	b_i
1	1589.516	0.268419	0
2	50.19525	1.220548	4.417455
3	20.91469	1.747258	17.66982
4	148.4943	4.406129	226.0978
5	1256.973	12.63	475.1397
6	9169	11.21284	4550.765

The RI data for 10-nm-size $CsPbBr_3$ quantum dots were given in [21] and listed in Table 3. For more precise calculation, the RI values were interpolated for each tested wavelength according to [21]. The transmission loss, α_{loss}, for the PCFs can be expressed as

Table 3 Parameters of $CsPbBr_3$ QDs from [21].

Wavelength (nm)	n	k
350	1.61761	0.138800
370	1.65585	0.140330
376	1.69187	0.141200
390	1.73672	0.140550
410	1.77602	0.138580
430	1.81184	0.134860
450	1.83820	0.133550
470	1.85419	0.131580
486	1.85215	0.133110
490	1.84326	0.134210
506	1.80928	0.146230
510	1.81750	0.148420
522	2.04067	0.102730
527	2.29889	0.029070
530	2.36556	0.014210
537	2.40437	0.005900
550	2.36918	0.001750
570	2.32196	0.001530
590	2.28026	0.001310
610	2.24396	0.001090
630	2.21469	0.000874
650	2.18895	0.000874
670	2.16327	0.000873
690	2.13594	0.000874
710	2.12060	0.000875
730	2.09165	0.000873
750	2.08315	0.000874

$$\alpha_{loss} = 8.686 \times k \, \mathrm{Im}[n_{eff}] \ \ (\mathrm{dB/cm}) \qquad (3)$$

where $\mathrm{Im}[n_{eff}]$ is the imaginary part of the effective index of the PCF core mode.

The electromagnetic mode of the PCF was solved with the finite element method fulfilled by COMSOL Multiphysics 5.6. The computation area was discretized by triangular subdomains, with a perfectly matched layer (PML) applied as the boundary layer. The simulation was terminated when the convergence equaled to or less than 1.0×10^{-6}.

3. Results and discussion

The loss spectra indicate the light energy dissipation of the core mode, and the peak loss takes place at the resonance wavelength (λ_m) with the most effective coupling between the core mode and the SPR mode of the Au layer (shortened as "SPR mode" hereinafter). In Fig. 1(b), the loss spectra for the sensors are demonstrated with n_a of the filled analyte being 1.30 (for other n_a values, the results are similar, which will be explained later). Correspondingly, electric field modulus distributions at the resonance wavelengths are depicted as the two inset figures above the peak loss in Fig. 1(b), from which it was found that the electric fields concentrated on the core mode of the PCFs for the Au sensors, whereas an apparent dispersion of the electric field towards the SPR mode upon the central holes could be observed for the QDs/Au sensors, contributing to the energy loss increasing and FWHM narrowing at λ_m, then the RI identification accuracies could be elevated. Though far from the resonance wavelengths, as the two inset figures in Fig. 1(b) at 425 nm and 725 nm, the electric field distributions for both types of the sensors were similar, and the core/SPR coupling was weak.

To further explore the RI sensing performances with the incorporation of the QDs layers in Au-coated PCF sensors, the loss spectra with the n_a values varied from 1.26 to 1.34 with a step of 0.01 were calculated for the QDs/Au and Au sensors

shown in Figs. 2(a) and 2(b), respectively. For both sensors, as n_a increases, λ_m shifts to longer wavelengths, caused by the elevation of the propagation constants of the SPR mode [30]. It must be mentioned that all the peak losses were within the visible region (from 629 nm to 705 nm for the QDs/Au sensors and from 505 nm to 555 nm for the Au sensors) in this sensing range, making the sensors convenient to operate compared to the RI sensors working at infrared regions [16, 25, 26]; $CsPbBr_3$ QDs have strong absorbance in the visible region, so QDs/Au sensor works better. Thus, for the n_a values larger than 1.34, the loss peak would enter the infrared region, which induced inconvenience for experimental fulfillment and the absorption for QD was weak, so this has not been explored in this work.

In addition, from Fig. 2(b), the peak loss of the Au sensors mounted with an increase in n_a, while that of the QDs/Au sensors firstly rose until n_a approaching to 1.30, then decreased slightly for larger n_a values, as shown in Fig. 2(a); the reason to explain this phenomenon could be that the contrast of the effective RI values between the core and SPR modes achieved the closest at n_a = 1.30 for the QDs/Au sensors, while it was continuously declined for the Au sensors and the peak loss did not reach the saturation point [13, 31, 32]. It is undesirable that, for n_a larger than 1.30, high order resonance peaks became obvious for the QDs/Au sensors [as shown in Fig. 2(a)] and may cause error identifications for the analytes.

To quantitatively evaluate the performance of the sensors, an "amplitude interrogation mode" was adopted, and with this mode, n_a identification could be fulfilled by detecting the loss amplitude variation at certain wavelength. Accordingly, amplitude sensitivity S_A is calculated as

$$S_A(\lambda,\ n_a) = (\Delta\alpha_{\text{loss}} / \Delta n_a) / \alpha_{1.30} \qquad (4)$$

where $\Delta\alpha_{\text{loss}}$ is the loss value changing due to the RI variation (Δn_a) near n_a, the length of the PCF is $1/\alpha_{1.30}$, and $\alpha_{1.30}$ denotes the loss value for n_a=1.30. S_A for other n_a values has been calculated, and the loss spectrum of n_a=1.30 is preferable since that high order resonance peak is weak, and the peak loss value is relatively large. Besides, it must be mentioned that in the amplitude interrogation mode, a light power meter should be equipped with the PCF sensors to measure the loss amplitude.

As shown in Fig. 2(c), the maximum value of S_A was 73.46 RIU^{-1} for the QDs/Au sensors at 675 nm, while it was 17.71 RIU^{-1} for the Au sensors at 555 nm. If the light power meter possessed a resolution of 1% change of the transmitted light intensity, it could guarantee a maximum RI resolution of 1.4×10^{-4} RIU for the QDs/Au sensors, though only 5.6×10^{-4} RIU for the Au sensors. The amplitude sensitivity was all positive for the Au sensors as shown in Fig. 2(c), while for the QDs/Au sensors, both negative and positive values appeared, and the reason is that the loss of the Au sensors rose with an increase in n_a from 1.26 to 1.33 for the whole wavelength range [from 400 nm to 700 nm, as shown in Fig. 2(b)]; as for the QDs/Au sensors, the trend of $\Delta\alpha_{\text{loss}}$ changing was less regular due to the loss spectra overlapping, as shown in Fig. 2(a).

Considering that the high order resonance may cause inaccurate RI identification for the QDs/Au sensors in the amplitude interrogation mode, hence "wavelength interrogation mode" was applied, with which the main peak could be easily distinguished from the high order peaks [32], and wavelength sensitivity, S_n, was adopted to evaluate the sensing performances:

$$S_n = \Delta\lambda_m / \Delta n_a \qquad (5)$$

where $\Delta\lambda_m$ is the resonance wavelength variation caused by the change of n_a, and λ_m needs to be distinguished by a spectrometer equipped to the PCFs.

As shown in Fig. 2(d), S_n was obtained from the slope of the linear fits of the λ_m-n_a data with an increasing step (Δn_a) of 0.01; and for the QDs/Au sensors, S_n was 947 nm/RIU, which gave an RI

detection resolution of 1.1×10^{-4} RIU if the spectral resolution of the spectrometer was 0.1 nm, while S_n for the Au sensors was 600 nm/RIU (RI detection resolution was 1.67×10^{-4} RIU). With QDs layers applied upon Au, the SPR propagation constants got larger [32], then the QDs/Au sensors worked at longer resonance wavelengths [Fig. 2(a)], which increased the plasmon penetration depth so that the evanescent field would be exposed to the surrounding environment more significantly, resulting in obvious λ_m shifting and S_n improving [33–35].

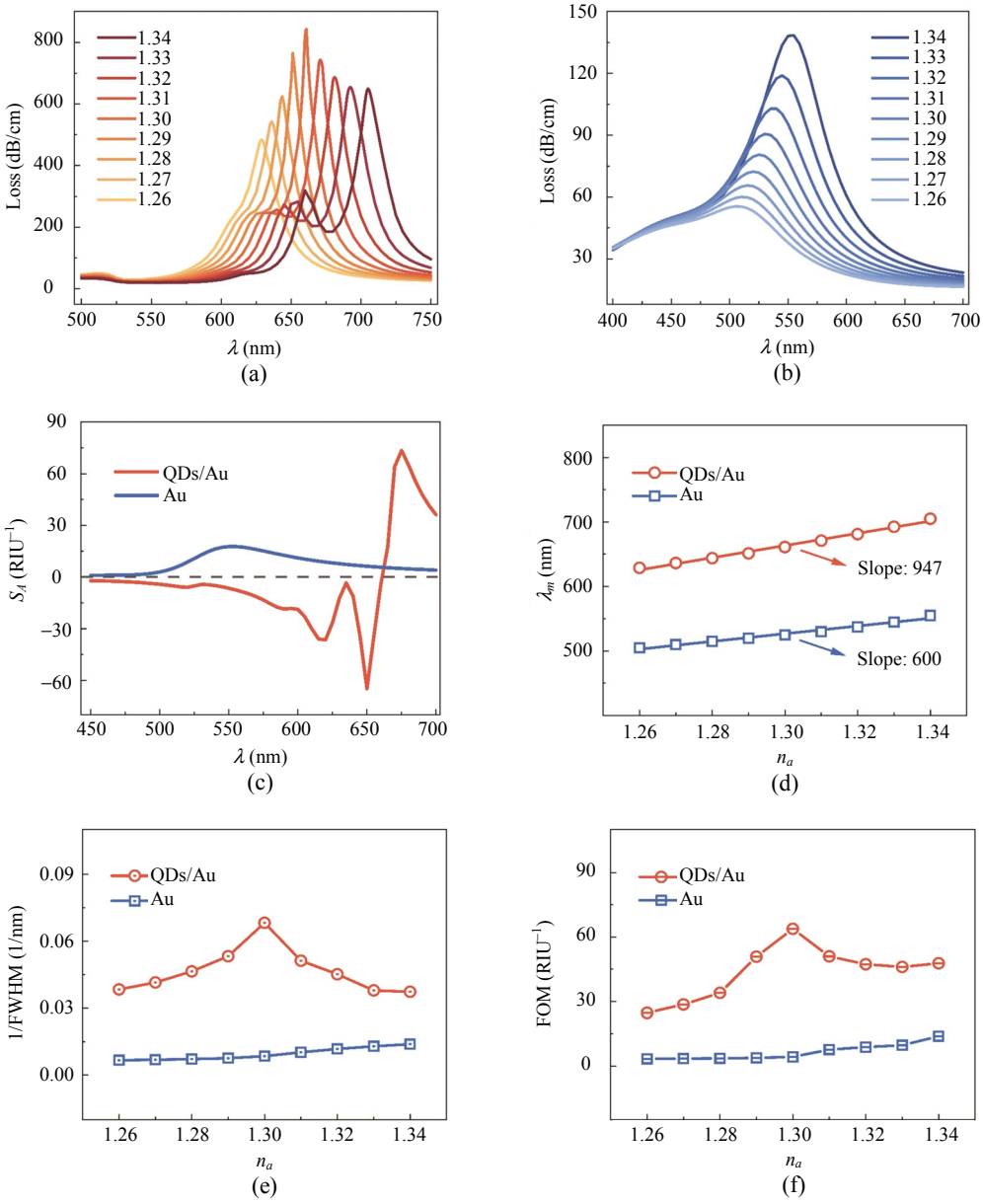

Fig. 2 Loss spectra for the QDs/Au sensors (a) and Au sensors (b) with different n_a and the performance comparisons: (c) amplitude sensitivity with n_a = 1.30, (d) wavelength sensitivity, (e) 1/FWHM, and (f) FOM.

Subsequently, the FWHM was measured as the difference between the wavelengths at which the loss values equaled to the half of the peak loss value in a loss spectrum (with the minimum loss value being subtracted). In Fig. 2(e), 1/FWHM instead of FWHM was adopted to perform a better comparison between the QDs/Au and Au sensors, and the QDs/Au sensors showed larger 1/FWHM values

(equivalently, narrower FWHM). Especially, the largest 1/FWHM was 0.064 6 nm^{-1} for the QDs/Au sensors (i.e., the smallest FWHM of 15.48 nm) with n_a=1.30, which was 4.65 times of the narrowest one of Au sensors (1/FWHM was 0.013 9 nm^{-1}, and FWHM was 72.05 nm with n_a=1.34).

Furthermore, FOM was calculated, which is defined as

$$\mathrm{FOM} = S_n / \mathrm{FWHM} . \quad (6)$$

It is straightforward that high S_n and narrow FWHM could result in large FOM values, which benefits the n_a identification. As shown in Fig. 2(f), the highest FOM value was 63.79 RIU^{-1} for the QDs/Au sensors with n_a=1.30 and 13.88 RIU^{-1} for the Au sensors at n_a=1.34. Here, S_n was obtained from (5), which was the variation rate of λ_m with Δn_a at n_a, other than the linear fit results as shown in Fig. 2(d), hence the calculation of FOM would be more accurate.

Furthermore, geometric factors (the layer number of the QDs, the thickness of the Au layers, and the diameter of the central holes) were investigated with n_a =1.30, at which the FWHM value was the smallest and the FOM was the highest for the QDs/Au sensors. Firstly, the Au thickness was kept as 30 nm and the layer number of the QDs was changed from 1 to 3. From the results in Fig. 3(a), λ_m had a redshift with the rise of the QDs thickness, and the sensors with 1-layer QDs exhibited a low peak loss value and wide FWHM (47.03 nm); contrast to the 2-layer QDs sensors, 3-layer QDs induced a high order resonance peak and larger FWHM at the main loss peak (19.86 nm). As a result, 2 layers should be the preferable thickness for the QDs and FWHM was the smallest (15.48 nm) along with a much weak high order resonance peak.

The thickness of the Au layer varied from 20 nm to 50 nm in the QDs/Au sensors, with the QDs layer kept as 2 layers (n_a still was 1.30). As shown in Fig. 3(b), λ_m had a redshift to longer wavelengths, and the peak loss value was the largest with the 30-nm-thick Au layer (meanwhile, FWHM was the narrowest), which could be explained that for thin Au layers (20 nm here) the oscillation density was deficient, while for thicker Au (40 nm and 50 nm) higher damping loss would occur and part of the core energy was sacrificed to overcome the damping loss [36, 37].

For comparison, the Au thickness in the Au sensors was also adjusted as shown in Fig. 3(c), and the Au sensors exhibited larger FWHM and much lower peak loss than those of the QDs/Au sensors with the same Au thickness as shown in Fig. 3(b) [the range of the vertical axis in Fig. 3(b) is 12 times larger than that of the Fig. 3(c)].

To evaluate the influences from the functional layer thickness on S_n, the $\Delta\lambda_m$-Δn_a relation of the sensors was investigated for n_a changed from 1.30 to 1.31 (for the narrowest FWHM at n_a = 1.30). In Figs. 3(d) and 3(e), λ_m increased by about 10 nm when Δn_a was 0.01 (and the sensitivity was about 1 000 nm/RIU); except that for 1 layer of QDs [Fig. 3(d)] or 20 nm Au cases [Fig. 3(e)], this value was about 8 nm, resulting from weak coupling and relatively short λ_m [31–33]. Moreover, as shown in Fig. 3(f), there was also no conspicuous influence on the λ_m change rate with Δn_a as the Au thickness varied for the Au sensors (S_n kept as ~500 nm/RIU). Therefore, S_n was insensitive to the thickness of the active layers as investigated here; consequently, the performance of sensors was determined mainly by the FWHM values, then 2-layer QDs and 30-nm-thick Au were the best option for the QDs/Au sensors in the current PCF structure, which was discussed in detail as shown in Fig. 2.

At last, the diameter of the central holes in the PCFs was changed from 0.51 μm (D–0.4L) to 2.55 μm (D+0.4L) with a step of 0.255 μm (0.1L) to investigate the influences on the performances of the sensors, while the diameter of other cladding holes remained unchanged as D. The thickness of the Au layer and the QDs layer number were 30 nm and

2 layers, respectively, in the QDs/Au sensors; the thickness of the Au layer in the Au sensors was 30 nm, as shown in Fig. 3(c), which could result in a high loss and a narrow FWHM.

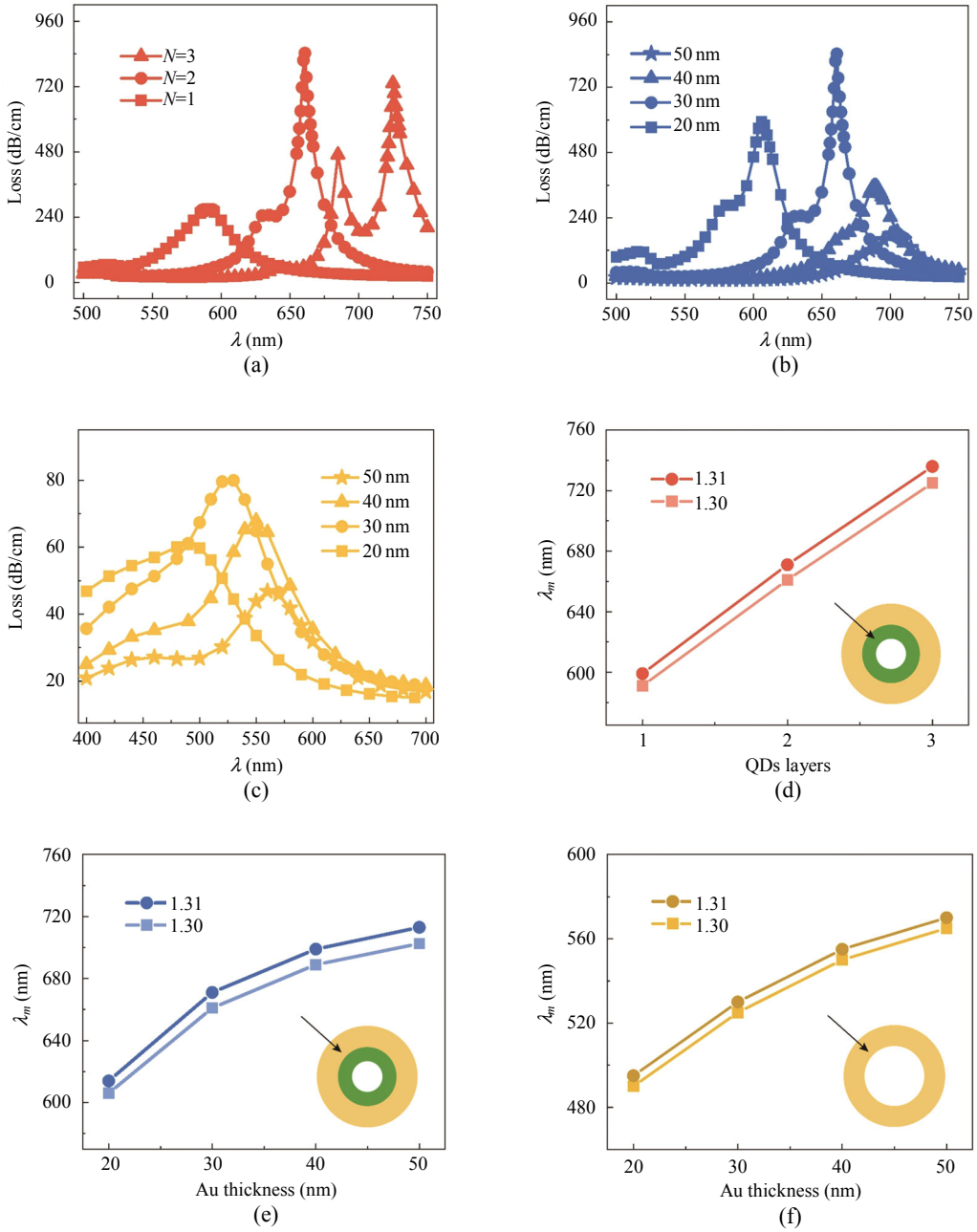

Fig. 3 Geometric parameter impacts on both kind of sensors: (a) and (b) loss spectra for the QDs/Au sensors with different layer numbers of QDs or thickness of Au; (c) loss spectra for the Au sensors with different thicknesses of Au; (d), (e), and (f)) corresponding peak positions to (a), (b), and (c) for n_a = 1.30 and 1.31, respectively. The insets indicate the part for the thickness variation.

In Fig. 4(a), central holes with larger sizes led to longer λ_m for the QDs/Au sensors; and in Fig. 4(b), the redshift of λ_m for the Au sensors was less obvious. An increase in the central hole size induced a closer proximity of the active layers to the core, which stimulated stronger core/SPR mode coupling, and the real part of the effective RI of the core mode diminished more evidently for the QDs/Au sensors at the phase matching point than that of the Au sensor [33]. Nevertheless, when the size was larger

than D+0.1L, there was another resonance peak appearing and mixed with the main peak [these curves were depicted separately in Fig. 5(a), leading to undistinguishable λ_m for the QDs/Au sensors and deteriorating the sensitivity in the wavelength interrogation mode]. The more intense coupling between the core and SPR modes may be the reason for the escalation of the energy loss towards the high order peaks [32].

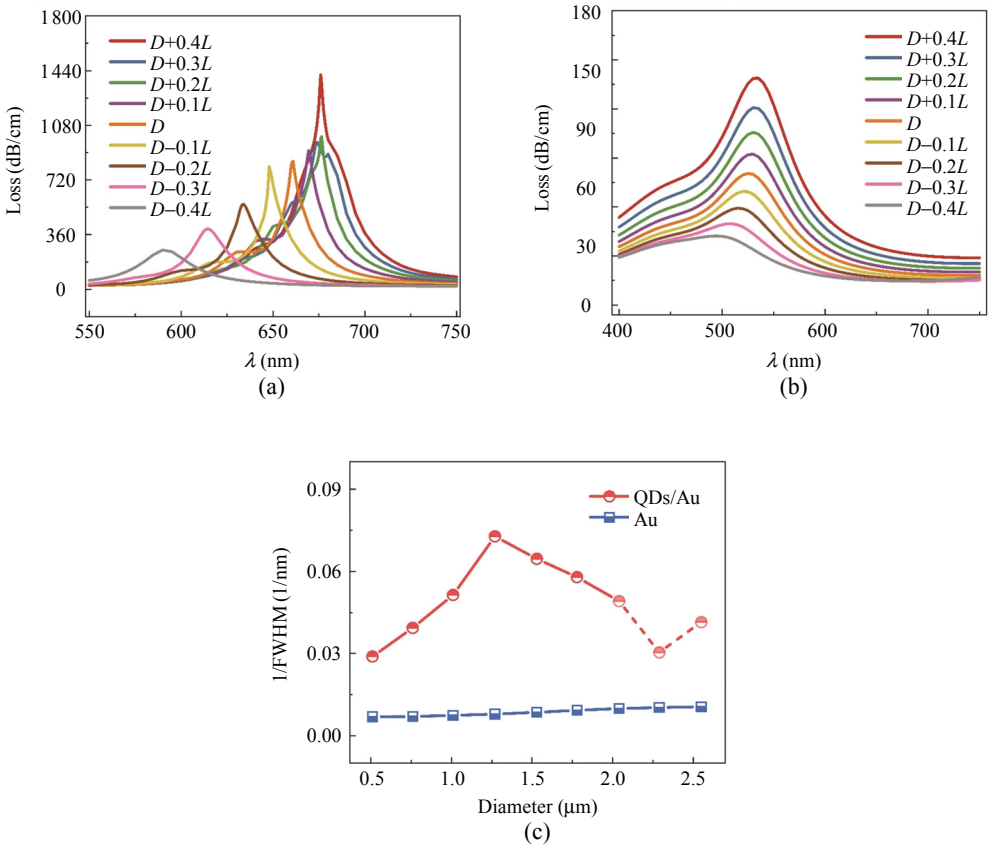

Fig. 4 Loss spectra for the QDs/Au sensors (a) and Au sensors (b) with different diameters for the central holes, and (c) results of 1/FWHM extracted from (a) and (b).

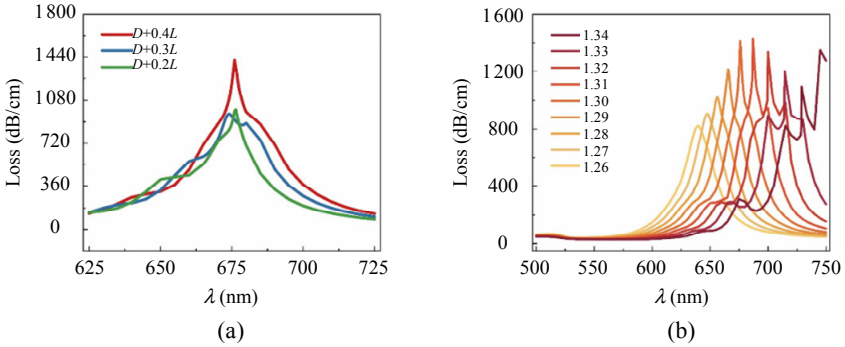

Fig 5 Extra information for geometric parameter impacts: (a) loss spectra for the hole size larger than D+0.1L at n_a = 1.30 and (b) loss spectra for D+0.4L with different n_a values.

As shown in Fig. 4(c), with the adjustment of the central hole sizes, the narrowest FWHM was obtained at D–0.1L (FWHM was 13.74 nm, and 1/FWHM = 0.072 8 nm^{-1}). In addition, when the size

was larger than D+0.1L, high order peaks mixed with the main peak, which brought difficulties to distinguish the main peaks and, actually, the FWHM values were calculated as the mixture of several peaks. Therefore, in Fig. 4(c), the 1/FWHM values for the central hole sizes larger than D+0.1L are displayed in faded color and connected by a dash line.

It must be emphasized that, as shown in Fig. 4(a) and Fig. 5(a), when the central hole size equaled D+0.4L, due to the high value of the peak loss, the curve showed a sharp shape, whereas because of the peak mixture, the real FWHM was not as high as it exhibits in the figure (which was 18.47 nm according to the same calculation method as the other loss spectra). Besides, considering that the peak mixture for D+0.4L was more severe than that of D+0.2L and D+0.3L, therefore, the loss spectra for D+0.4L at different n_a values were explored in detail as shown in Fig. 5(b); it was found that when n_a increased to 1.30, another peak close to the main peak appeared; there were even two high order peaks appearing when n_a was larger than 1.31, which affected the wavelength sensitivity adversely.

From Fig. 4(c), FWHM approached the smallest value as 13.74 nm at D–0.1L; accordingly, the wavelength sensitivity and FOM for different n_a from 1.26 to 1.34 were calculated as shown in Fig. 6; the linear fit sensitivity and highest FOM were 850 nm/RIU and 60.06 RIU at n_a=1.30, respectively.

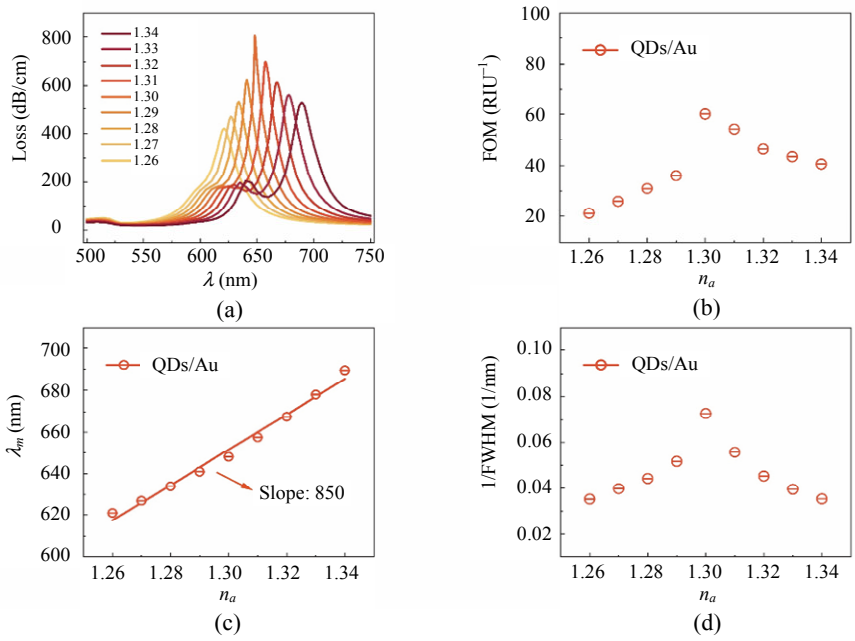

Fig. 6 Sensor performances for the central hole size equaling D–0.1L for different n_a: (a) the loss spectra, (b) FOM, (c) peak position and corresponding linear fit result, and (d) 1/FWHM.

The performance comparison of this work to other PCF RI sensors is provided in Table 4. Although the sensitivity was still low, the QDs/Au sensors in this work achieved quite narrow FWHMs and showed the potential for the detection of low-RI analytes. Besides, the triangular-lattice PCF is the most adopted structure in PCFs, so it is convenient to make real prototype of PCFs-RI sensors. With rational design of the PCF structures, such as to adopt H-shaped, D-shaped, or other asymmetric PCFs, the sensitivity and FOM could be further improved. To confirm this point, the D-shaped PCF according to Ref. [33] was also calculated as shown in Fig. 7. It is obvious that the sensitivity was

improved compared to the triangular-lattice PCF RI sensors [800 nm/RIU for D-shaped Au sensor and 1 900 nm/RIU for the D-shaped QDs/Au sensor with n_a changing from 1.26 to 1.27, higher than 500 nm/RIU and 750 nm/RIU for Au sensor and QDs/Au sensor based on triangular-lattice PCFs, respectively, as calculated from Fig. 2(d)].

Table 4 Performance comparison with other works.

Ref.	n_a range	S_n (nm/RIU)	FOM (RIU^{-1})	FWHM (nm)
[20]	1.33 to 1.39	7540.00	280.00	27.00
[24]	1.29 to 1.39	116000.00	2320.00	50.00
[38]	1.333 to 1.380	2557.00	15.00	170.00
[39]	1.332 to 1.382	3627.51	53.00	81.00
[40]	1.33 to 1.38	3499.00	46.00	76.00
[41]	1.4772 to 1.5116	12500.00	150.00	83.00
[42]	1.22 to 1.37	51000.00	566.00	90.11
This work§	1.26 to 1.34	947.00	63.79	15.48
This work§§	1.26 to 1.34	850.00	60.06	13.74

§ The central hole size was D;
§§ The central hole size was D–0.1L.

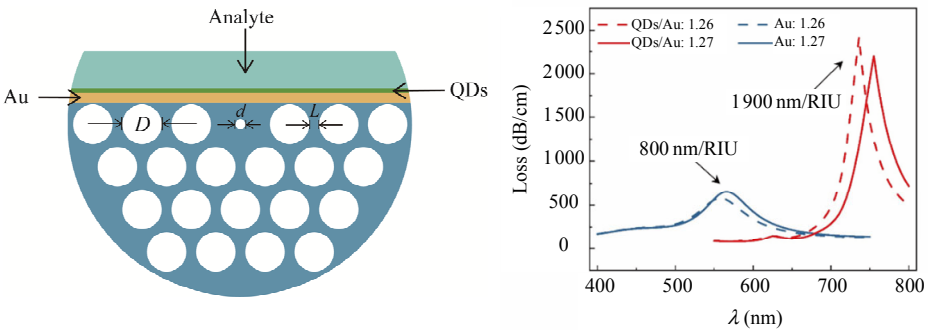

(a) (b)

Fig. 7 Simulation results for D-shaped PCF: (a) schematic illustration of the PCF RI sensor coated with the Au and QDs films on the polished surface of D-shaped fiber: D=1.6 μm, d=0.4 μm, and L=0.4 μm; (b) loss spectra for QDs/Au and Au sensors when n_a was set to be 1.26 and 1.27.

4. Conclusions

In this work, $CsPbBr_3$ QDs layers were applied as the dielectric layer upon Au, together coated on the sidewalls of the central holes in triangular-lattice PCFs. It was found that the existence of the $CsPbBr_3$ QDs could enhance the energy transfer from the core mode to the SPR mode, improving the sensing performances in both the amplitude and wavelength interrogation modes. Moreover, geometric parameters were adjusted to achieve the best sensing abilities. It is believed that with the rational design of the PCF structures or inserting a dielectric layer beneath Au could further improve the sensitivity meanwhile keeping the narrow FWHM of the QDs/Au sensors.

Acknowledgment

This work was supported by National Key Research and Development Program of China (Grant No. 2016YFA0202401); National Natural Science Foundation of China (Grant No. 61705066); Open Fund of IPOC (BUPT) (Grant No. IPOC2018B004); Fundamental Research Funds for the Central Universities, China (Grant No. 2020JG002).

References

[1] R. C. Jorgenson and S. S. Yee, "A fiber-optic chemical sensor based on surface plasmon resonance," *Sensors and Actuators B: Chemical*, 1993, 12(3): 213–220.

[2] E. G. Neumann, "*The fundamental fiber mode*," in Single-Mode Fibers: Fundamentals, H. K. V. Lotsch, Ed. Berlin Heidelberg: Springer-Verlag, 1988: 88.

[3] M. Erdmanis, D. Viegas, M. Hautakorpi, S. Novotny, J. L. Santos, and H. Ludvigsen, "Comprehensive numerical analysis of a surface-plasmon-resonance sensor based on an H-shaped optical fiber," *Optics Express*, 2011, 19(15): 13980–13988.

[4] Z. Fan, S. Li, Q. Liu, G. An, H. Chen, J. Li, *et al.*, "High sensitivity of refractive index sensor based on analyte-filled photonic crystal fiber with surface plasmon resonance," *IEEE Photonics Journal*, 2015, 7(3): 1–9.

[5] X. Guo, "Surface plasmon resonance based biosensor technique: a review," *Journal of Biophotonics*, 2012, 5(7): 483–501.

[6] W. Qin, S. Li, Y. Yao, X. Xin, and J. Xue, "Analyte-filled core self-calibration microstructured optical fiber based plasmonic sensor for detecting high refractive index aqueous analyte," *Optics and Lasers in Engineering*, 2014, 58: 1–8.

[7] B. Shuai, L. Xia, Y. Zhang, and D. Liu, "A multi-core holey fiber based plasmonic sensor with large detection range and high linearity," *Optics Express*, 2012, 20(6): 5974–5986.

[8] L. Zheng, X. Zhang, X. Ren, J. Gao, L. Shi, X. Liu, *et al.*, "Surface plasmon resonance sensors based on Ag-metalized nanolayer in microstructured optical fibers," *Optics & Laser Technology*, 2011, 43(5): 960–964.

[9] M. M. Rahman, M. A. Molla, A. K. Paul, M. A. Based, M. M. Rana, and M. S. Anower, "Numerical investigation of a highly sensitive plasmonic refractive index sensor utilizing hexagonal lattice of photonic crystal fiber," *Results in Physics*, 2020, 18: 103313.

[10] M. A. Mahfuz, M. A. Mollah, M. R. Momota, A. K. Paul, A. Masud, S. Akter, *et al.*, "Highly sensitive photonic crystal fiber plasmonic biosensor: design and analysis," *Optical Materials*, 2019, 90: 315–321.

[11] Q. Liu, J. Sun, Y. Sun, Z. Ren, C. Liu, J. Lv, *et al.*, "Surface plasmon resonance sensor based on photonic crystal fiber with indium tin oxide film," *Optical Materials*, 2020, 102: 109800.

[12] M. Rycenga, C. M. Cobley, J. Zeng, W. Li, C. H. Moran, Q. Zhang, *et al.*, "Controlling the synthesis and assembly of silver nanostructures for plasmonic applications," *Chemical Reviews*, 2011, 111(6): 3669–3712.

[13] X. Shui, Q. Gu, X. Jiang, and G. Si, "Surface plasmon resonance sensor based on polymer liquid-core fiber for refractive index detection," *Photonics*, 2020, 7(4): 123–134.

[14] J. Lu, Y. Li, Y. Han, Y. Liu, and J. Gao, "D-shaped photonic crystal fiber plasmonic refractive index sensor based on gold grating," *Applied Optics*, 2018, 57(19): 5268–5272.

[15] S. Qiu, J. Yuan, X. Zhou, F. Li, Q. Wang, Y. Qu, *et al.*, "Hollow-core negative curvature fiber with high birefringence for low refractive index sensing based on surface plasmon resonance effect," *Sensors (Basel)*, 2020, 20(22): 6539–6551.

[16] J. R. Guzmán-Sepúlveda, R. Guzmán-Cabrera, M. Torres-Cisneros, J. J. Sánchez-Mondragón, and D. A. May-Arrioja, "A highly sensitive fiber optic sensor based on two-core fiber for refractive index measurement," *Sensors (Basel, Switzerland)*, 2013, 13(10): 14200–14213.

[17] S. Jiao, S. Gu, H. Fang, and H. Yang, "Analysis of dual-core photonic crystal fiber based on surface plasmon resonance sensor with segmented silver film," *Plasmonics*, 2018, 14(3): 685–693.

[18] X. Yang, Y. Lu, M. Wang, and J. Yao, "SPR sensor based on exposed-core grapefruit fiber with bimetallic structure," *IEEE Photonics Technology Letters*, 2016, 28(6): 649–652.

[19] N. M. Y. Zhang, K. Li, P. P. Shum, X. Yu, S. Zeng, Z. Wu, *et al.*, "Hybrid graphene/gold plasmonic fiber-optic biosensor," *Advanced Materials Technologies*, 2017, 2(2): 1600185.

[20] N. Gomez-Cardona, E. Reyes-Vera, and P. Torres, "High sensitivity refractive index sensor based on the excitation of long-range surface plasmon polaritons in H-shaped optical fiber," *Sensors (Basel)*, 2020, 20(7): 2111–2121.

[21] S. Yakunin, L. Protesescu, F. Krieg, M. I. Bodnarchuk, G. Nedelcu, M. Humer, *et al.*, "Low-threshold amplified spontaneous emission and lasing from colloidal nanocrystals of caesium lead halide perovskites," *Nature Communications*, 2015, 6(1): 8056.

[22] F. Juan, F. Xu, M. Wang, M. Wang, G. Hou, J. Xu, *et al.*, "Photoluminescence enhancement of perovskite $CsPbBr_3$ quantum dots by plasmonic Au nanorods," *Chemical Physics*, 2020, 530: 110627.

[23] M. Gong, M. Alamri, D. Ewing, S. M. Sadeghi, and J. Z. Wu, "Localized surface plasmon resonance enhanced light absorption in AuCu/$CsPbCl_3$ Core/Shell nanocrystals," *Advanced Materials*, 2020,

32(26): 2002163.
[24] E. Haque, S. Mahmuda, M. A. Hossain, N. H. Hai, Y. Namihira, and F. Ahmed, "Highly sensitive dual-core PCF based plasmonic refractive index sensor for low refractive index detection," *IEEE Photonics Journal*, 2019, 11(5): 1–9.
[25] F. Wang, C. Liu, Z. Sun, T. Sun, B. Liu, and P. K. Chu, "A highly sensitive SPR sensors based on two parallel PCFs for low refractive index detection," *IEEE Photonics Journal*, 2018, 10(4): 1–10.
[26] X. Chen, L. Xia, and C. Li, "Surface plasmon resonance sensor based on a novel D-shaped photonic crystal fiber for low refractive index detection," *IEEE Photonics Journal*, 2018, 10(1): 1–9.
[27] X. Yang, Y. Lu, B. Liu, and J. Yao, "Simultaneous measurement of refractive index and temperature based on SPR in D-shaped MOF," *Applied Optics*, 2017, 56(15): 4369–4374.
[28] L. Zhao, H. Han, Y. Lian, N. Luan, and J. Liu, "Theoretical analysis of all-solid D-type photonic crystal fiber based plasmonic sensor for refractive index and temperature sensing," *Optical Fiber Technology*, 2019, 50: 165–171.
[29] M. De and V. K. Singh, "Magnetic fluid infiltrated dual core photonic crystal fiber based highly sensitive magnetic field sensor," *Optics & Laser Technology*, 2018, 106: 61–68.
[30] Y. Xu, P. Bai, X. Zhou, Y. Akimov, C. E. Png, L. K. Ang, *et al.*, "Optical refractive index sensors with plasmonic and photonic structures: promising and inconvenient truth," *Advanced Optical Materials*, 2019, 7(9): 1801433.
[31] M. S. Aruna Gandhi, K. Senthilnathan, P. R. Babu, and Q. Li, "Visible to near infrared highly sensitive microbiosensor based on surface plasmon polariton with external sensing approach," *Results in Physics*, 2019, 15: 102590.
[32] N. N. Luan, R. Wang, Y. Lu, and J. Q. Yao, "Simulation of surface plasmon resonance temperature sensor based on liquid mixture-filling microstructured optical fiber," *Optical Engineering*, 2014, 53(6): 067103.
[33] N. Luan, R. Wang, W. Lv, and J. Yao, "Surface plasmon resonance sensor based on D-shaped microstructured optical fiber with hollow core," *Optics Express*, 2015, 23(7): 8576–8582.
[34] D. Liu, A. K. Mallik, J. Yuan, C. Yu, G. Farrell, Y. Semenova, *et al.*, "High sensitivity refractive index sensor based on a tapered small core single-mode fiber structure," *Optics Letters*, 2015, 40(17): 4166–4169.
[35] G. Brambilla, F. Xu, P. Horak, Y. Jung, F. Koizumi, N. P. Sessions, *et al.*, "Optical fiber nanowires and microwires: fabrication and applications," *Advances in Optics and Photonics*, 2009, 1(1): 107–161.
[36] T. Li, L. Zhu, X. Yang, X. Lou, and L. Yu, "A refractive index sensor based on H-shaped photonic crystal fibers coated with Ag-graphene layers," *Sensors (Basel)*, 2020, 20(3): 741–750.
[37] S. Singh and Y. K. Prajapati, "TiO_2/gold-graphene hybrid solid core SPR based PCF RI sensor for sensitivity enhancement," *Optik*, 2020, 224: 165525.
[38] T. Hu, Y. Zhao, and A. N. Song, "Fiber optic SPR sensor for refractive index and temperature measurement based on MMF-FBG-MMF structure," *Sensors and Actuators B: Chemical*, 2016, 237: 521–525.
[39] Q. Wang, J. Jing, X. Wang, L. Niu, and W. Zhao, "A D-shaped fiber long-range surface plasmon resonance sensor with high *Q*-factor and temperature self-compensation," *IEEE Transactions on Instrumentation and Measurement*, 2020, 69(5): 2218–2224.
[40] Q. Wang, J. Jing, W. Zhao, X. Fan, and X. Wang, "A novel fiber-based symmetrical long-range surface plasmon resonance biosensor with high quality factor and temperature self-reference," *IEEE Transactions on Nanotechnology*, 2019, 18: 1137–1143.
[41] X. Zhao, X. Zhang, X. S. Zhu, and Y. W. Shi, "Long-range surface plasmon resonance sensor based on the GK570/Ag coated hollow fiber with an asymmetric layer structure," *Optics Express*, 2019, 27(7): 9550–9560.
[42] E. Haque, M. A. Hossain, Y. Namihira, and F. Ahmed, "Microchannel-based plasmonic refractive index sensor for low refractive index detection," *Applied Optics*, 2019, 58(6): 1547–1554.